

COMMUNICATION

**High tap density microparticles of selenium-doped germanium as a high efficiency, stable cycling lithium-ion battery anode material**

Cite this: DOI: 10.1039/x0xx00000x

Received 00th January 2012,  
Accepted 00th January 2012

DOI: 10.1039/x0xx00000x

[www.rsc.org/](http://www.rsc.org/)

Kyle C. Klavetter,<sup>a,†</sup> J. Pedro de Souza,<sup>a,†</sup> Adam Heller,<sup>a</sup> and C. Buddie Mullins<sup>c,\*</sup>

## COMMUNICATION

**Materials and Methods**

**Synthesis of  $\text{Ge}_{0.9}\text{Se}_{0.1}$  and pure Ge.** In a typical synthesis of  $\text{Ge}_{0.9}\text{Se}_{0.1}$ , 4.46 g Ge (Lesker, 99.999% pure, 3-6 mm pieces) and 0.54 g Se (Lesker, 99.999% pure, 1-3 mm pieces) were set inside quartz ampoule (GM Associates, Inc., 8mm ID, 12 mm OD) previously cleaned (by rinsing with acetone and drying) and sealed at one end. The ampoule was evacuated to  $10^{-6}$  torr and carefully sealed *c.* 12 cm from its end. The ampoule was then heated to  $1100^\circ\text{C}$  at  $5^\circ\text{C min}^{-1}$  and held at  $1100^\circ\text{C}$  for 48 h inside a quartz tube continuously rotated in a tube furnace (Lindberg Blue M, single zone). The continuous rotation was achieved using a home-built rotational tube drive and gently rocked the ampoules, promoting the mixing of Ge and Se as suggested by the study done by Ross and Bourgon.<sup>1</sup> The synthesis temperature of  $1100^\circ\text{C}$  was selected so as to form a single liquid phase of  $\text{Ge}_{0.9}\text{Se}_{0.1}$ . Rapid quenching was performed by dropping the ampoule into a room temperature water bath. Approximately 10 seconds or less elapsed between when the ampoule was directly in the furnace hot zone and when the ampoule was fully submerged under water. After allowing the ampoule to fully cool, the ampoule was scored and opened: a slight “pop” was heard upon opening which verified that the ampoule was properly sealed and held vacuum during the high temperature mixing synthesis. Note on safety: on one occasion, the ampoule may have been improperly sealed and when it was opened without allowing for its contents to fully cool, the odor of rotted eggs was detected, indicating the presence of the very hazardous  $\text{H}_2\text{Se}$  gas. The synthesis of the pure Ge was performed in a similar way, except that the ampoule contained only Ge pieces, the ampoule was scaled to a longer length to accommodate 25 g of Ge and the hold time at  $1100^\circ\text{C}$  was limited to 12 h because there was no need to mix the ampoule contents.

**Production of microsized particles.** The contents of the ampoules were carefully removed and then quickly crushed into roughly uniform pieces by pestle and mortar. This material was fed into a jet mill (Glen Mills, Jet-O-Mizer Model 00) operated at 100 psi feed pressure, 80 psi pusher pressure and with  $\text{N}_2$  as the feed and pusher gas. The rate of feed was *c.*  $0.25\text{-}0.5\text{ g min}^{-1}$  and managed using a vibratory feeder fitted with a custom 3D printed part designed to regulate particle flow rate. Greater than 80 percent yield was obtained using a home-built collection apparatus. Because the particle size distribution of jet milled materials is a function of the material properties, the initial size distribution of the material and the feed rate, the material was processed twice. The first run processed feed material of comparatively wide particle size distribution made from coarse crushing with a pestle and mortar. The design of the jet mill only allows product particles of below a certain size to escape the milling chamber and for Ge-type materials this size is *c.* 10 microns at the largest. Thus, for the second run of processing, the feed material was of a relatively narrow size distribution. The total time for processing was about 20-40 minutes per run with about 20 minutes required to carefully retrieve the powder from the home-built collection apparatus.

**The advantages of jet milling.** Jet milling is a commercially used process already employed for production of lithium-ion battery (LIB) materials. Importantly, jet milling is a process which can be easily scaled from lab processing (several grams per hour) to commercial processing (many tons per hour). Jet milling has several advantages:<sup>5</sup> one, it allows for contamination-free product as the grinding is done by particle on particle collision. For this reason, high purity materials such as those used in the pharmaceutical, electronics and battery materials industries. Two, the particle size and size distribution can be controlled. In this study, we report on particles of an average size of about 2-3 microns and with SEM (Fig. S1†) we observed, as expected, a low content of fines, small particles which are common in ball milled materials. However, with expertise and custom-tuning of the mill (particularly the feed rate), the particle size can be lowered by up to an order of magnitude and the size distribution can be narrowed. For example, the Jet Pulverizer Company developed a jet mill process in 2009<sup>6</sup> to create high-purity lithium titanate oxide of less than 300 nm average size. Should we find in subsequent studies that solid state diffusion of lithium is the limiting factor in the  $\text{Ge}_{0.9}\text{Se}_{0.1}$  particles tested in this study, then we might anticipate that the electrochemical performance of a 300 nm sized  $\text{Ge}_{0.9}\text{Se}_{0.1}$  particle could be improved by more than a magnitude of order, retaining 80% capacity at 10C or more rather than at 1C as demonstrated in Fig. 1. Note: Jet milling units such as the one used in this study can be rented on a month-to-month basis rather than purchased outright and are simple enough for undergraduate research assistants to set up and operate.

**Particle characterization. (Fig. S1-4)** Tap density measurements on the  $\text{Ge}_{0.9}\text{Se}_{0.1}$  and the pure Ge powders (after the jet milling process described above) were performed using a Quantachrome AT-4 Autotap machine. Powder XRD measurements were performed using a Rigaku MiniFlex 600 (Fig. S2†). SEM characterization was performed using a Hitachi S5500 SEM/STEM at 30kV and 20  $\mu\text{A}$  on powders dispersed by bath sonication in ethanol and dropped onto lacey carbon TEM grids (SPI Supplies). EDS measurements were performed using the STEM mode on the Hitachi S5500. The particles of  $\text{Ge}_{0.9}\text{Se}_{0.1}$  and pure Ge were found to be uncontaminated by the quartz ampoule, the jet mill (316 stainless steel) and with negligible oxygen content (Fig. S4†). EDS spectra, line scans and mapping were performed on the  $\text{Ge}_{0.9}\text{Se}_{0.1}$  particles to assess the degree of mixing of the Ge and Se. The EDS line scans for the  $\text{Ge}_{0.9}\text{Se}_{0.1}$  particles are composed of thousands of discrete measurements of elemental composition. These data are plotted in a histogram (Fig. S3†) alongside a representative EDS mapping of several particles. A bimodal distribution was observed with the majority of the material characterized as the desired  $\text{Ge}_{0.9}\text{Se}_{0.1}$  mixture and a minority of the material characterized as a GeSe-like material, slightly rich in Ge,  $\text{Ge}_{0.6}\text{Se}_{0.4}$ . Owing to the large dimension of the particles characterized, only several seconds of EDS signal collection were necessary to achieve a stable spectra, helping to minimize the error associated with this measurement technique.

**Electrochemical testing by galvanostatic cycling. (Fig. S5-6)** A typical slurry was composed of 0.8 g active material (pure Ge or  $\text{Ge}_{0.9}\text{Se}_{0.1}$  particles), 0.1 g Super P Li conductive additive (Timcal) and 0.1 g carboxymethyl cellulose (Sigma, 90 kDa, pre-dissolved in water) in water. Mixing was done in two stages: first using an IKA ULTRA-TURRAX tube drive homogenizer and second using a probe sonicator (QSonica microtip, pulses at 20 percent amplitude, 1 s on, 1 s off for 20 min) with the slurry container cooled by a water bath. The slurry was cast on 10  $\mu\text{m}$  thick Cu foil (MTI), allowed to air dry and then dried overnight under vacuum at 100°C. Electrodes were punched with a 7/16 inch diameter and measured to 0.01 mg (Mettler Toledo). In an Ar-filled glovebox (MBRAUN,  $\text{H}_2\text{O}$  and  $\text{O}_2$  less than 0.1 ppm), 2032 coin cells were constructed using Celgard 2400 membrane separators, 0.75 mm thick Li foil (Alfa) and 1M  $\text{LiPF}_6$  (BASF) in 1:1 (volume ratio) FEC (Solvay):DEC (Alfa, 99.9% anhydrous). Cells were allowed to rest for at least 6 hours prior to commencing room temperature (*c.* 25°C) galvanostatic testing on an Arbin BT 2043 with a voltage window of 10 mV to 1.5 V. Each test began with an initial cycle at *C*/20 to condition the electrode. The pure Ge-based electrodes were tested using 1,384  $\text{mAh g}^{-1}$  as the theoretical capacity. The  $\text{Ge}_{0.9}\text{Se}_{0.1}$  electrodes were tested using 1,205  $\text{mAh g}^{-1}$  as the theoretical capacity because only Ge is active within the voltage range used. Plots of cycling performance as shown with capacity measured specific to the weight of the active material, either pure Ge or  $\text{Ge}_{0.9}\text{Se}_{0.1}$ . Eight electrodes of similar mass loading (0.54-0.70  $\text{mg cm}^{-2}$ ) were tested to indicate the performance of the pure Ge particles (Fig. S5c,f†). Fifteen electrodes of similar mass loading (0.54-0.67  $\text{mg cm}^{-2}$ ) were tested to indicate the performance of the  $\text{Ge}_{0.9}\text{Se}_{0.1}$  particles (Fig. S5a-b,d-e†). Five of the 15  $\text{Ge}_{0.9}\text{Se}_{0.1}$  electrodes were cycled to show an additional 100 cycles at 1C following the 80 cycle variable *C*-rate test and three of these five electrodes were cycled an additional 320 cycles for a total of 500 cycles of testing. All cell testing indicated good repeatability of the electrode performance. For the plot of galvanostatic cycling performance in the communication (Fig. 1), electrodes of about average performance were selected as representative of the other cell data and the pure Ge based electrode had a mass loading of 0.54  $\text{mg cm}^{-2}$  and the  $\text{Ge}_{0.9}\text{Se}_{0.1}$  electrode had a mass loading of 0.58  $\text{mg cm}^{-2}$ . First cycle voltage profiles for the pure Ge and the  $\text{Ge}_{0.9}\text{Se}_{0.1}$  particles are shown in Fig. S6†.

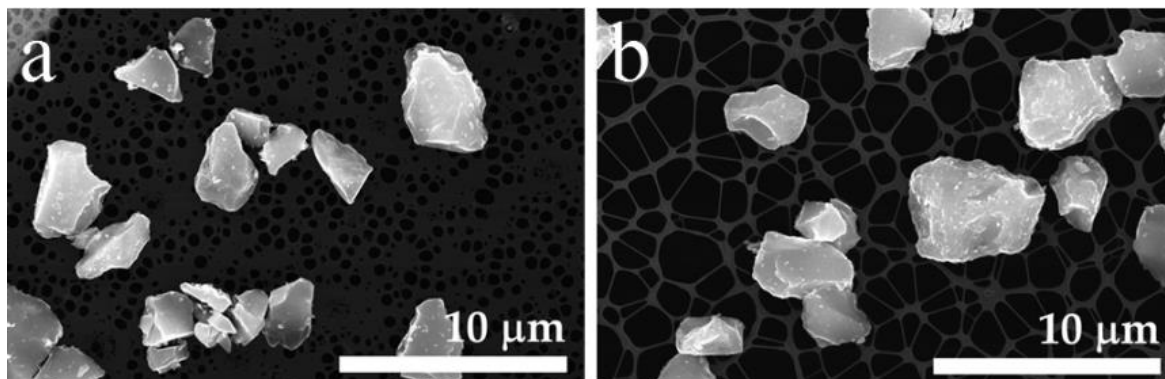
**Scanning electron microscopy (SEM). (Fig. S7-10)** SEM was conducted to examine the change in condition of the electrodes made with either pure Ge or  $\text{Ge}_{0.9}\text{Se}_{0.1}$  active material before and after cycling. In this study, the pristine (uncycled) electrodes were compared with cycled electrodes in the charged or discharged state following the 80 cycle variable *C*-rate test. The cycled electrodes were carefully removed from the 2032 coin cells by gently prying open one end of the 2032 cell using a pair of plastic pliers (I-V Products). The electrodes were then rinsed in DEC (Alfa) to remove the  $\text{LiPF}_6$  before being dried. The electrodes were exposed to air for several minutes before entry into the SEM. This is not believed to impact the morphology of the film. Note: a few solvents (acetic acid based, hydrochloric acid based) were employed in unsuccessful attempts to remove the SEI to expose the active material beneath without doing obvious damage to the film. Shown below are additional SEM and EDS of the pure Ge-based and the  $\text{Ge}_{0.9}\text{Se}_{0.1}$ -based electrodes in the pristine state, +80 cycles in charged state and +80 cycles in discharged state.

**Transmission electron microscopy (TEM). (Fig. S11-16)** TEM on a JEOL 2010F was conducted to examine the change in condition of the particles within the electrodes made with either pure Ge or  $\text{Ge}_{0.9}\text{Se}_{0.1}$  active material before and after cycling. In this study, the electrodes were examined in the discharged state following the 80 cycle variable *C*-rate test. The cycled electrodes were carefully removed from the 2032 coin cells by gently prying open one end of the 2032 cell using a pair of plastic pliers (I-V Products) inside the Ar-filled glovebox. The electrodes were then rinsed in DEC (Alfa) to remove the  $\text{LiPF}_6$  before being dried inside the Ar-filled glovebox. A razor blade was used to cut a sliver of the electrode *c.* 1 cm long by 0.25 mm thick which was set into a silicone mould. While still inside the Ar-filled glovebox, resin (812, Electron Microscopy Supplies) was poured around the suspended sliver of electrode and the resin was allowed to harden at 90°C for 48 h. The resin-embedded electrode sliver was then sectioned by ultramicrotome. The thickness of the sections cut by diamond knife edge (DIATOME) was set to *c.* 50 nm and a lacey carbon grid (SPI Supplies) was used to catch the sections while floating on water. It is likely

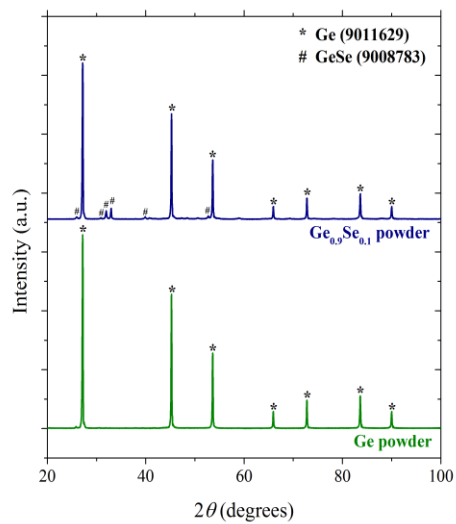
that the exposure of the outside of the section to water and air chemically contaminated the sample. To what extent is unknown. However, it is our belief that this is the most efficient and least contaminating method available to provide insight into the interior of the cycled electrode, particularly for this study which focuses upon the structural changes in the particles which are unlikely to be noticeably altered by exposure to water or air. We further note that in a previous study, this method successfully allowed for viewing of dendrites<sup>2</sup>, indicating that the resin safely preserves the material which is not directly exposed to the air or water. Lastly, we found that the large, micro-sized particles studied here were observed to often crack, possibly due to the cut made by the diamond knife, something which we sometimes observed in the course of a previous study<sup>7</sup>.

**High angle annular dark field (HAADF) scanning transmission electron microscopy (STEM).** (Fig. S11-16) A STEM beam of 1 nm was employed for HAADF-STEM images and EDS analysis of the sectioned electrodes. This technique is suited for providing more clear insight into the interior structure of the particles studied. By resolving signal as a function of thickness of sample (assumed constant due to the sectioning technique employed for sample preparation), density and atomic number ( $Z$ ) of material (signal intensity scales as a function of about  $Z^2$ , the carbonaceous polymer/SEI/conductive additive can be effectively masked. High contrast (bright/white signal) indicates regions of high density/high  $Z$ . Additionally, this technique enabled study of the phase segregation in the  $\text{Ge}_{0.9}\text{Se}_{0.1}$  because of the high signal given from the crystalline (high density) nano-inclusions of Ge (high  $Z$ ) surrounding the amorphous (lower density) Ge-Se-Li containing phase.

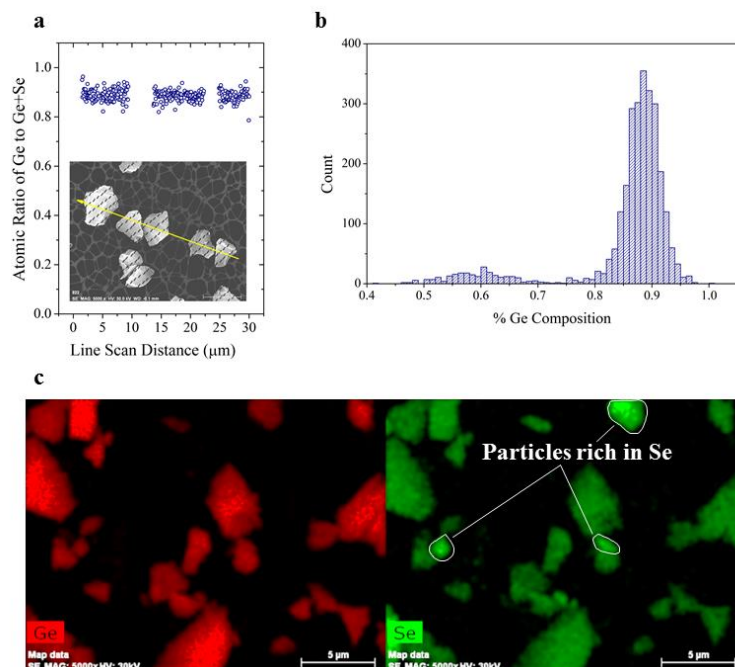
**Electrochemical impedance spectroscopy (EIS).** (Fig. S17) EIS was performed on a CHI 608D from 100 kHz to 0.01 Hz with 5 mV perturbation. The spectra were collected at a state of full discharge at open circuit potential on 2032 cells tested through the 80 cycle variable  $C$ -rate test. The low frequency data was analysed by fitting to a Warburg impedance element. The available electrochemically active surface area,  $a$ , was estimated by (i) assuming the electroactive material remaining was indicated by the 1C capacity, (ii) assuming that the average particle size was 2 microns in diameter and (iii) assuming spherical particles. Alternatively, by assuming the electrochemically active surface area was the electrode geometric area, a similar difference in diffusion coefficient values would be obtained. The differential potential to differential change in  $x$ , the amount of Li in the  $\text{Li}_x\text{Ge}$  phase, was obtained using the voltage profile of the 80<sup>th</sup> cycle in the variable  $C$ -rate test. The slope of the voltage profile near full discharge is relatively constant. Given these assumptions, the difference in the diffusion coefficients was estimated and found to be orders of magnitude different, as might be indicated by the different slopes of the low frequency EIS data:  $c. 10^{-11} \text{ cm}^2 \text{ s}^{-1}$  for the cycled  $\text{Ge}_{0.9}\text{Se}_{0.1}$  and  $c. 10^{-16} \text{ cm}^2 \text{ s}^{-1}$  for the cycled pure Ge.



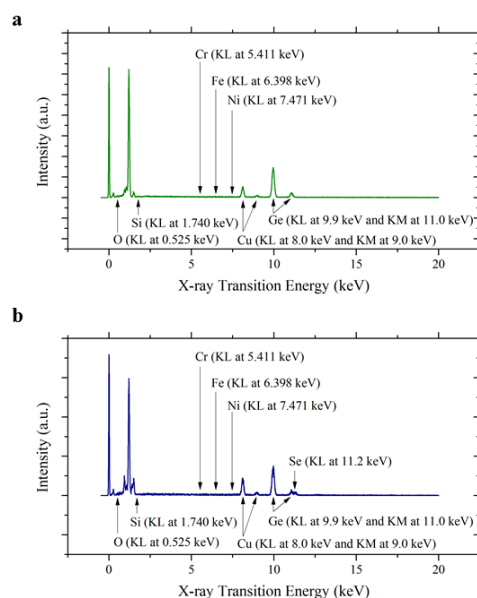
**Fig. S1.** (a) Pure Ge micro-sized particles produced from jet milling. (b) Ge<sub>0.9</sub>Se<sub>0.1</sub> micro-sized particles produced from jet milling.



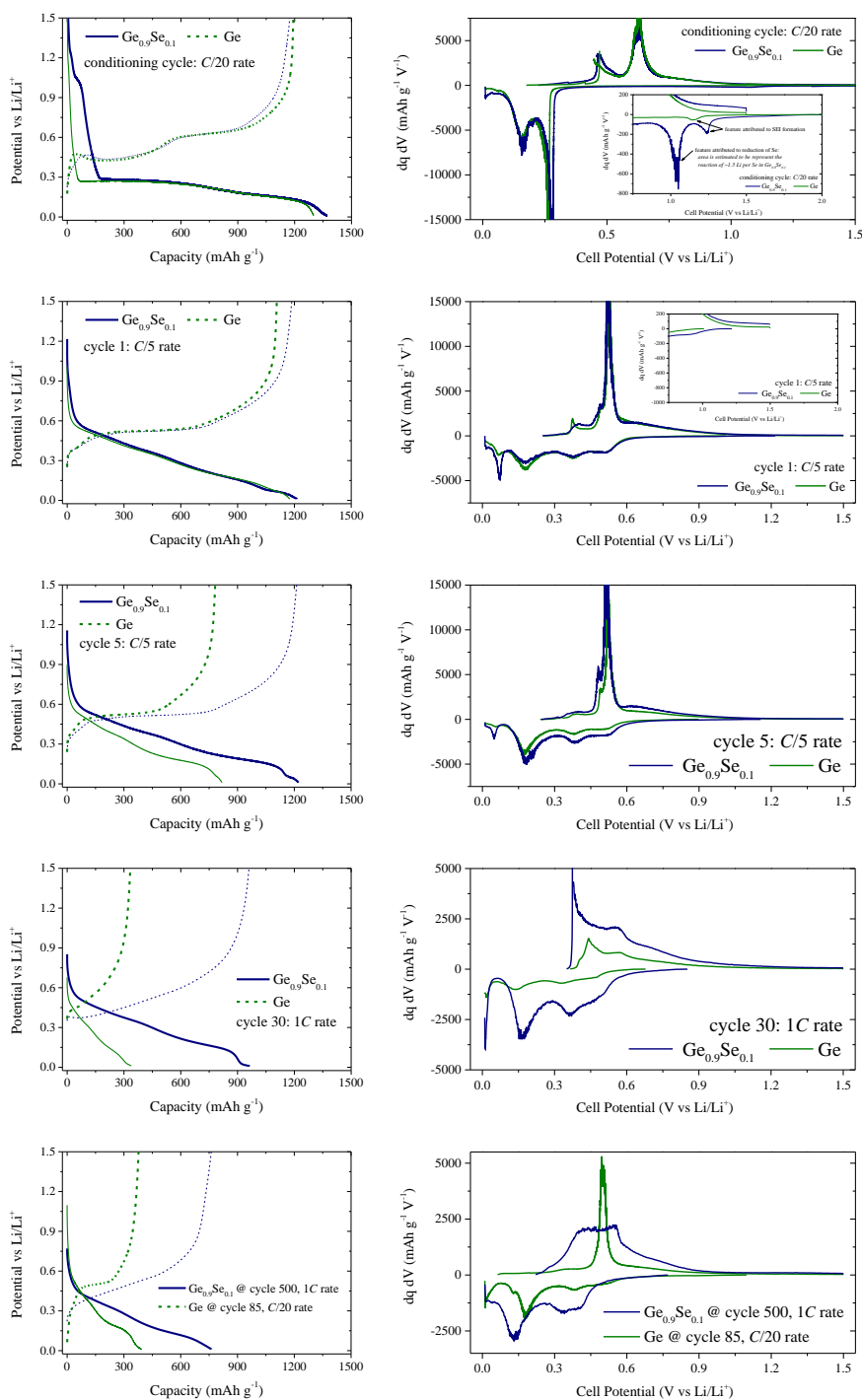
**Fig. S2.** Powder XRD of (a) Ge<sub>0.9</sub>Se<sub>0.1</sub> micro-sized particles produced from jet milling and (b) pure Ge micro-sized particles produced from jet milling.



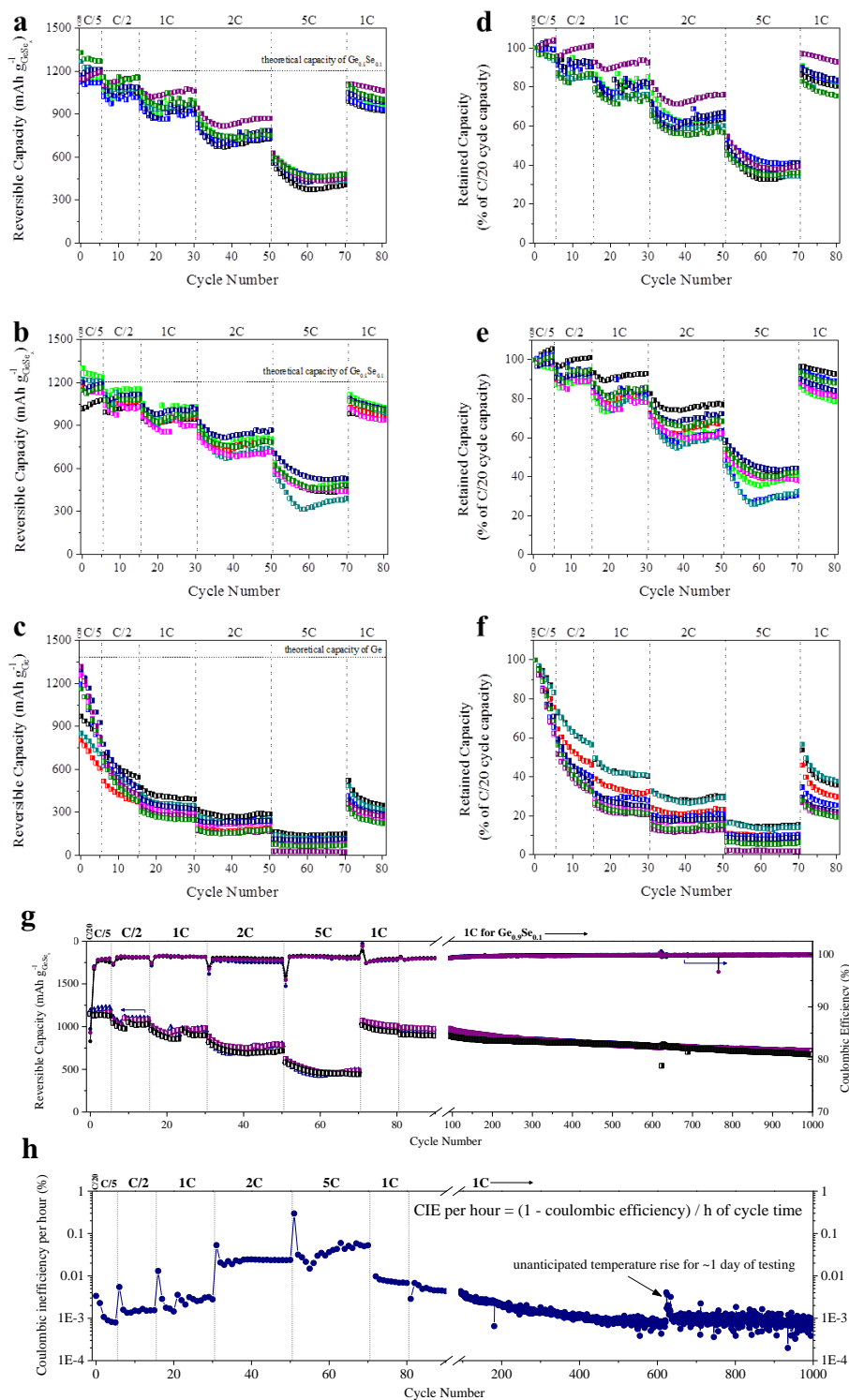
**Fig. S3.** (a) Typical EDS line scan of  $\text{Ge}_{0.9}\text{Se}_{0.1}$  particles after jet milling showing EDS line path and the corresponding elemental ratio of Ge to Ge+Se recorded. (b) Histogram reflecting thousands of discrete EDS point measurements analysed as a ratio of Ge to Ge+Se. A bimodal distribution is observed, with the majority of the material reflecting the desired  $\text{Ge}_{0.9}\text{Se}_{0.1}$  composition and a minority reflecting a GeSe-like phase, slightly rich in Ge. (c) Typical EDS map confirming that the majority of the particles are in the desired  $\text{Ge}_{0.9}\text{Se}_{0.1}$  mixture and that a minority of particles are Se-rich.



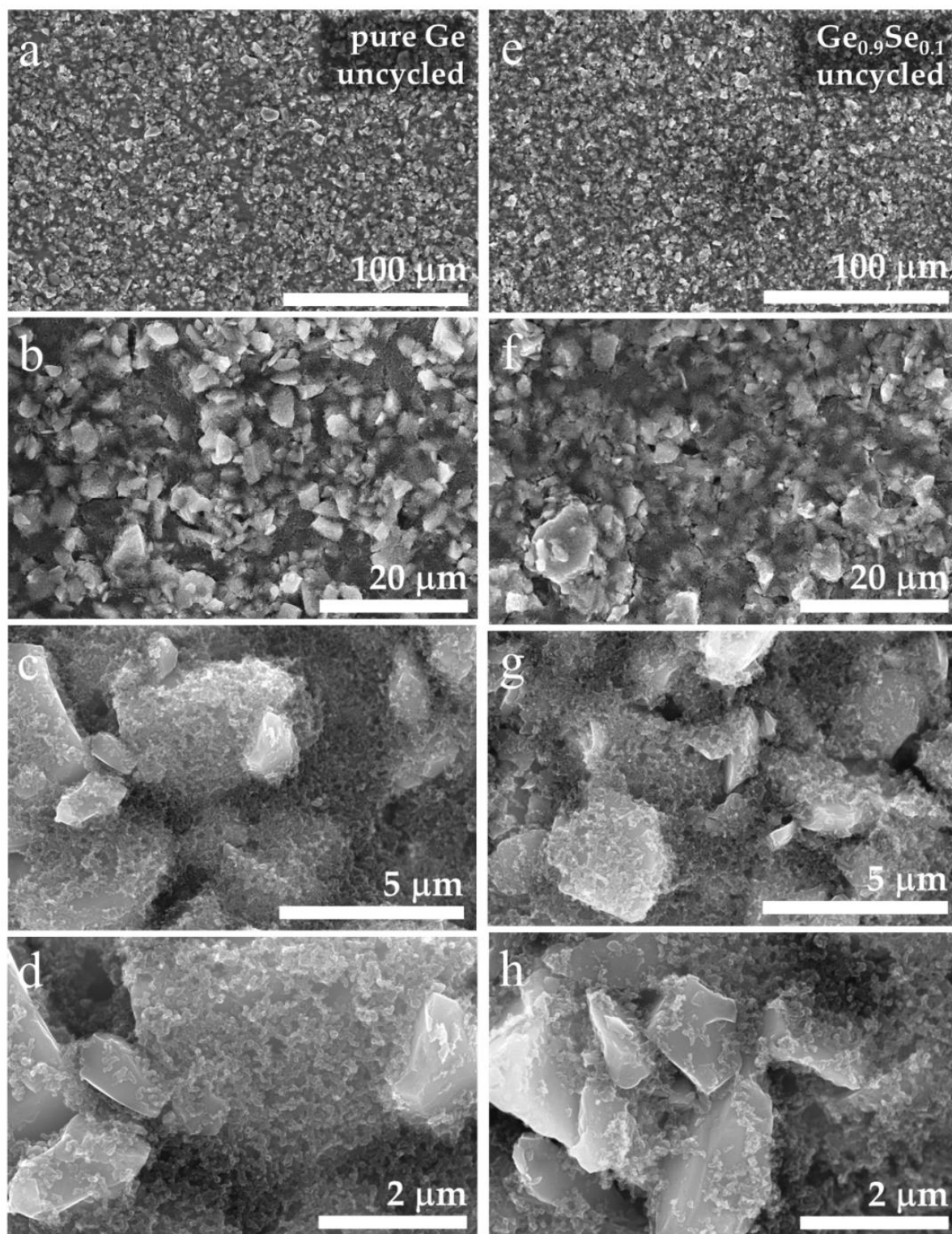
**Fig. S4.** Typical EDS spectrum characterizing many particles of (a) pure Ge and (b)  $\text{Ge}_{0.9}\text{Se}_{0.1}$  particles. Arrows are drawn to indicate the locations of the dominant x-ray transition energies for the desired elements, Ge or Ge and Se, as well as for potential contaminants. Contamination from the ampoule was not found as indicated by the absence of Si; contamination from the jet milling process was not found as indicated by the absence of Cr, Fe and Ni; and contamination from oxidation was negligible as indicated by the nearly undetectable O signal.



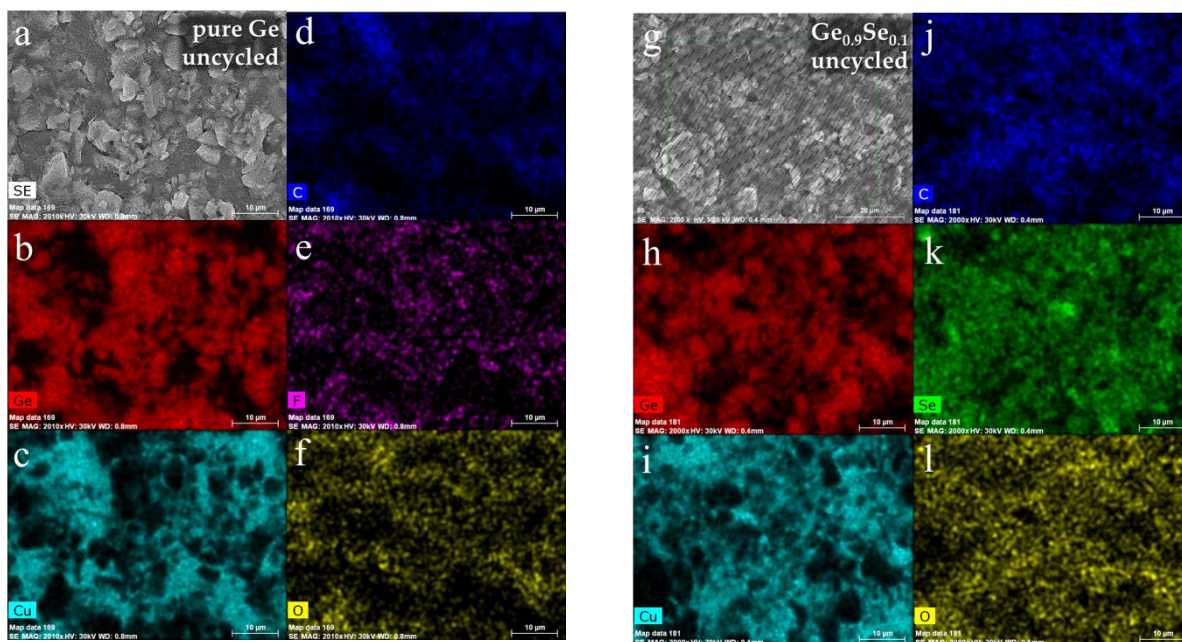
**Fig. S5.** Voltage profiles and corresponding differential capacity profiles for the pure Ge and the  $\text{Ge}_{0.9}\text{Se}_{0.1}$  based electrodes. Shown above are the conditioning cycle, 1<sup>st</sup> cycle (at C/5 rate), 5<sup>th</sup> cycle (at C/5 rate), 30<sup>th</sup> cycle (at 1C rate), and 500<sup>th</sup> cycle ( $\text{Ge}_{0.9}\text{Se}_{0.1}$  at 1C rate) or 85<sup>th</sup> cycle (pure Ge at C/20 rate). For the conditioning cycle, there is a lower capacity and larger irreversible loss in the  $\text{Ge}_{0.9}\text{Se}_{0.1}$ -based electrode due to the irreversible reaction of Li with Se (shown in inset graph to the differential capacity profile) which is not seen subsequently. The reaction pathway for the  $\text{Ge}_{0.9}\text{Se}_{0.1}$  appears nearly identical to that for the pure Ge, indicating that the Se reduces into an inactive phase.



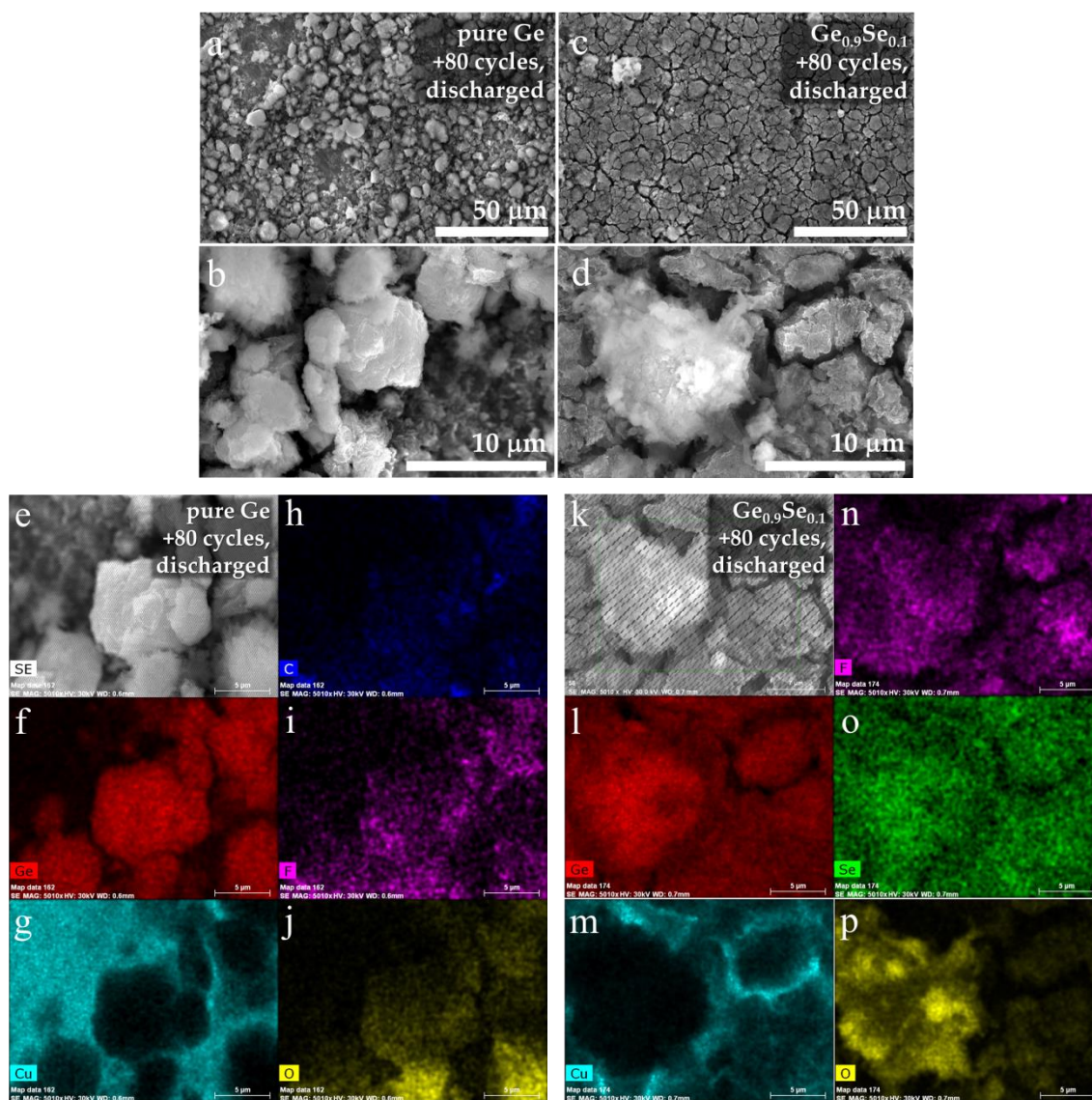
**Fig. S6.** Galvanostatic cycling performance of cells showing repeatability of data shown in Fig. 1 of the communication. Specific capacity vs cycle number for  $\text{Ge}_{0.9}\text{Se}_{0.1}$  cells (15 total) shown in (a) and (b) and corresponding graphs (d) and (e) of the capacity retention measured as a percent of the first cycle discharge (Li-extraction) capacity when testing was done at C/20. Specific capacity vs cycle number for the pure Ge cells (8 total) shown in (c) and corresponding graph (f) of the capacity retention measured as a percent of the first cycle discharge (Li-extraction) capacity when testing was done at C/20. Figure (g) shows the repeatability of the three  $\text{Ge}_{0.9}\text{Se}_{0.1}$  cells tested until 500 cycles. (h) The coulombic inefficiency per hour (CIE/h) of cycle time for the  $\text{Ge}_{0.9}\text{Se}_{0.1}$  electrode result shown in Fig. 1. The data is limited by the accuracy of the Arbin battery tester used which we estimate measures the coulombic efficiency to an accuracy of *c.* 0.1 percent. For a point of reference, the reader is referred to one of Dahn's recent studies<sup>3</sup> of commercial graphite-based batteries for which the CIE/h of cycle time is at least two orders of magnitude lower ( $10^{-5}$  CIE/h) than what is observed for the  $\text{Ge}_{0.9}\text{Se}_{0.1}$  based electrode studied here.



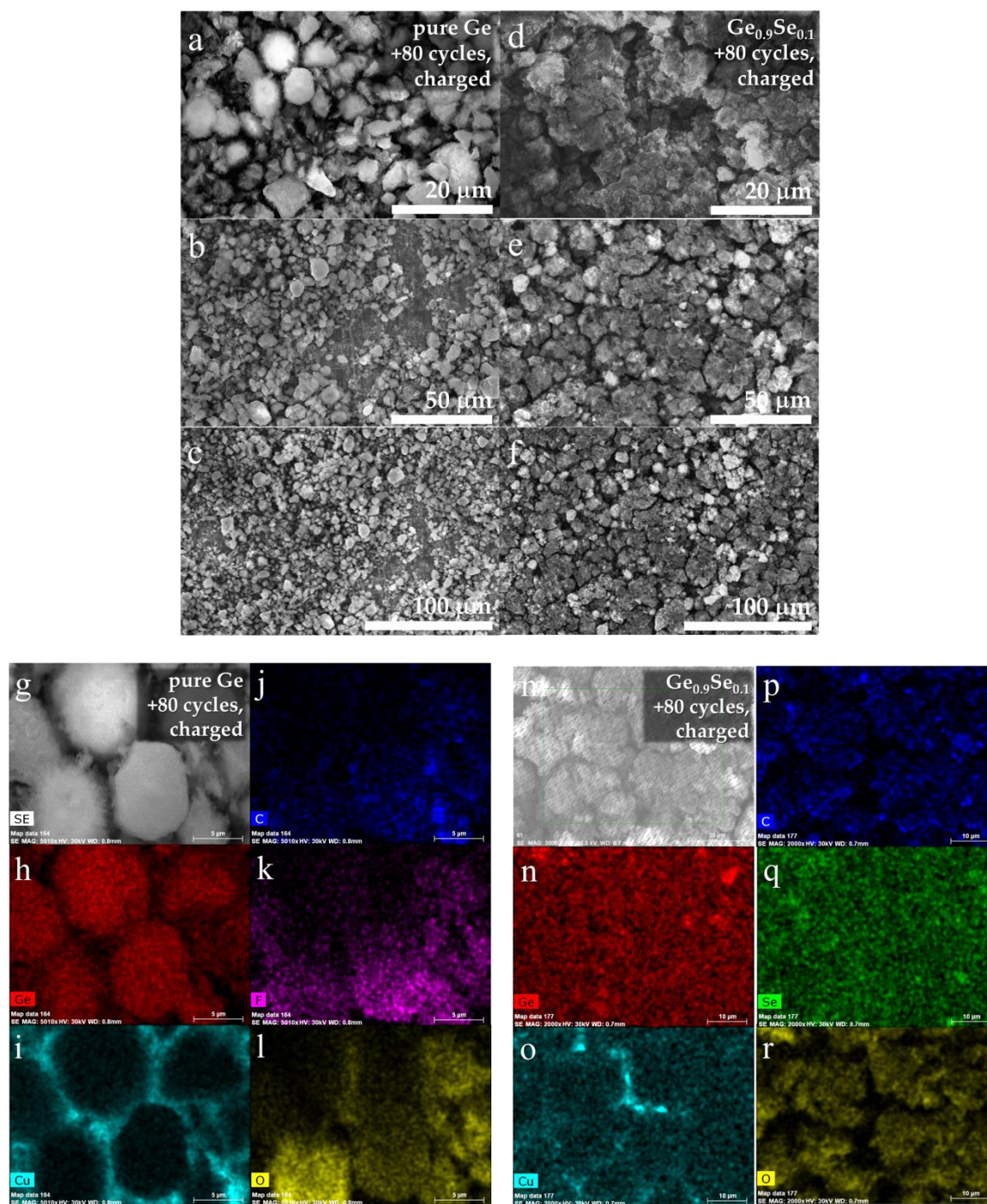
**Fig. S7.** SEM of pristine (uncycled) electrodes made using the pure Ge (a-d) or  $\text{Ge}_{0.9}\text{Se}_{0.1}$  (e-h) as the active material. The electrodes appear indistinguishable with similar particle size and degree of mixing and spacing of the larger, micro-sized active material particles and the smaller, conductive additive particles.



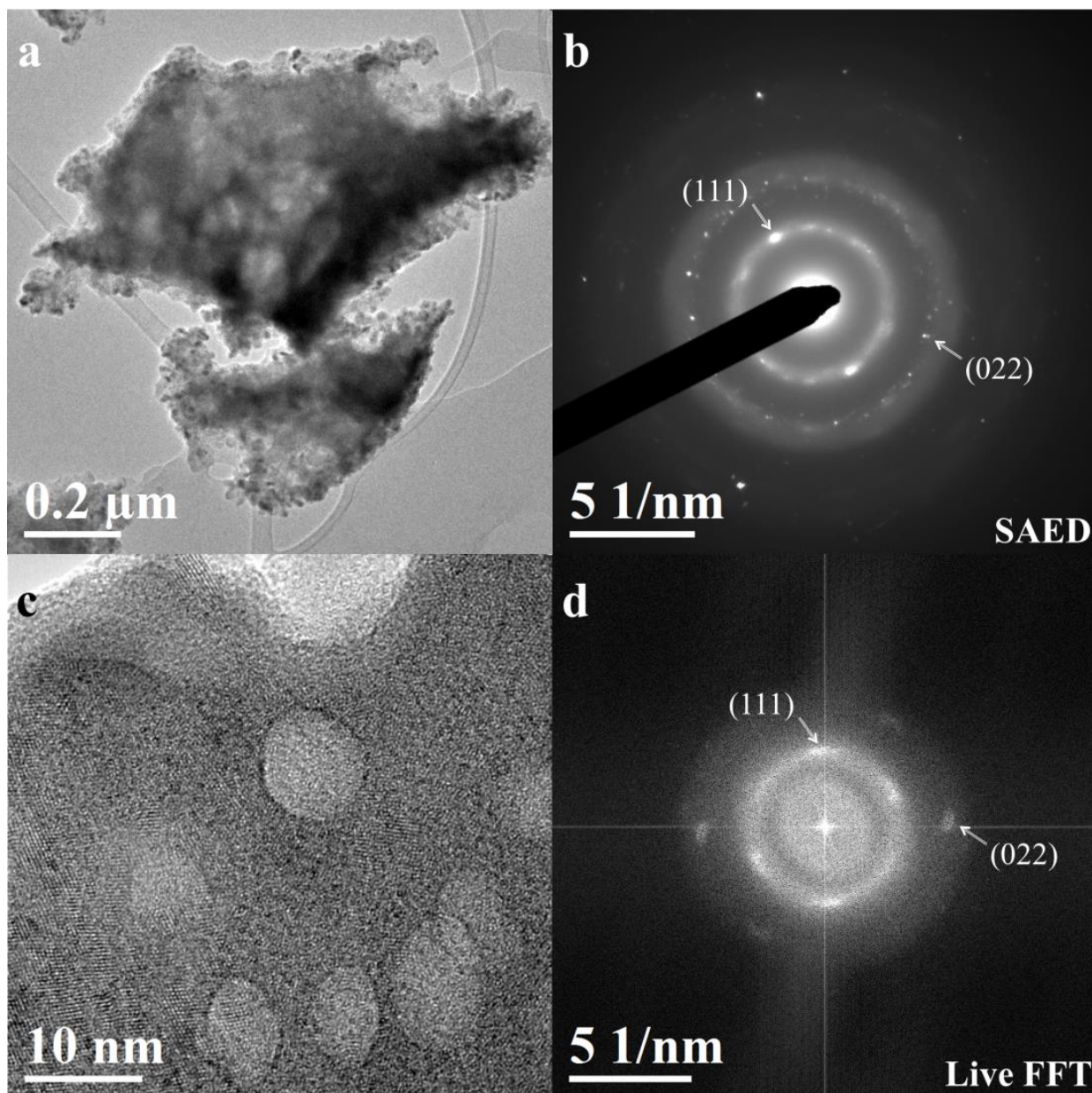
**Fig. S8.** EDS mapping of pristine (uncycled) electrodes made using the pure Ge (a-f) or  $\text{Ge}_{0.9}\text{Se}_{0.1}$  (g-l) as the active material. The electrodes appear indistinguishable with similar degree of mixing. Using Castaing's formula, the analysis depth (for Ge or  $\text{Ge}_{0.1}\text{Se}_{0.1}$ ) is estimated to be less than  $4\ \mu\text{m}$  for the beam conditions (30kV).



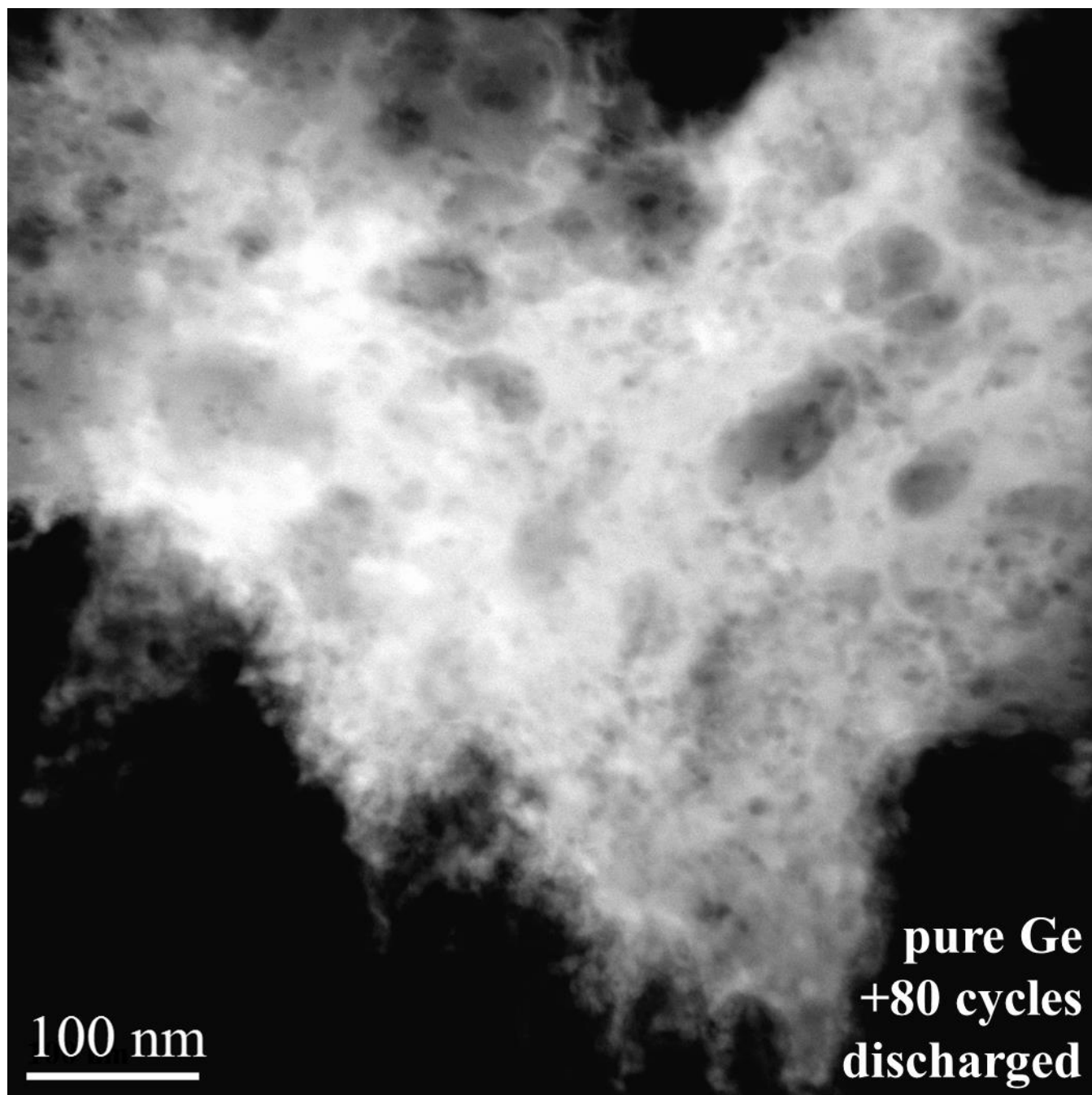
**Fig. S9.** SEM and EDS mapping of cycled electrodes (+80 cycles, after the variable *C*-rate test, discharged state) with the pure Ge (SEM: a-b, EDS: e-j) or Ge<sub>0.9</sub>Se<sub>0.1</sub> (SEM: c-d, EDS:k-p) as the active material. The EDS mapping for the cycled (discharged) pure Ge based electrode (e-j) shows a region which shows the border of delaminated film, clearly indicated by the EDS signal for the Ge (active material) and the Cu (substrate). The cycled film is covered in SEI and also in dendritic growths, these characterized by their structure (similar to what has been reported previously<sup>2</sup>) and high content of O which would be present in the decomposition species formed on the highly reactive lithium metal surfaces. The EDS mapping for the cycled (discharged) Ge<sub>0.9</sub>Se<sub>0.1</sub> based electrode (k-p) focuses upon one of the few dendritic growths observed on this film and is similarly identified by a particularly high O signal. As expected, the major dendritic growths are typically found on top of active material, indicating a local “hot zone” where the flux of lithium exceeds the rate at which it can transport into and react within the active material.



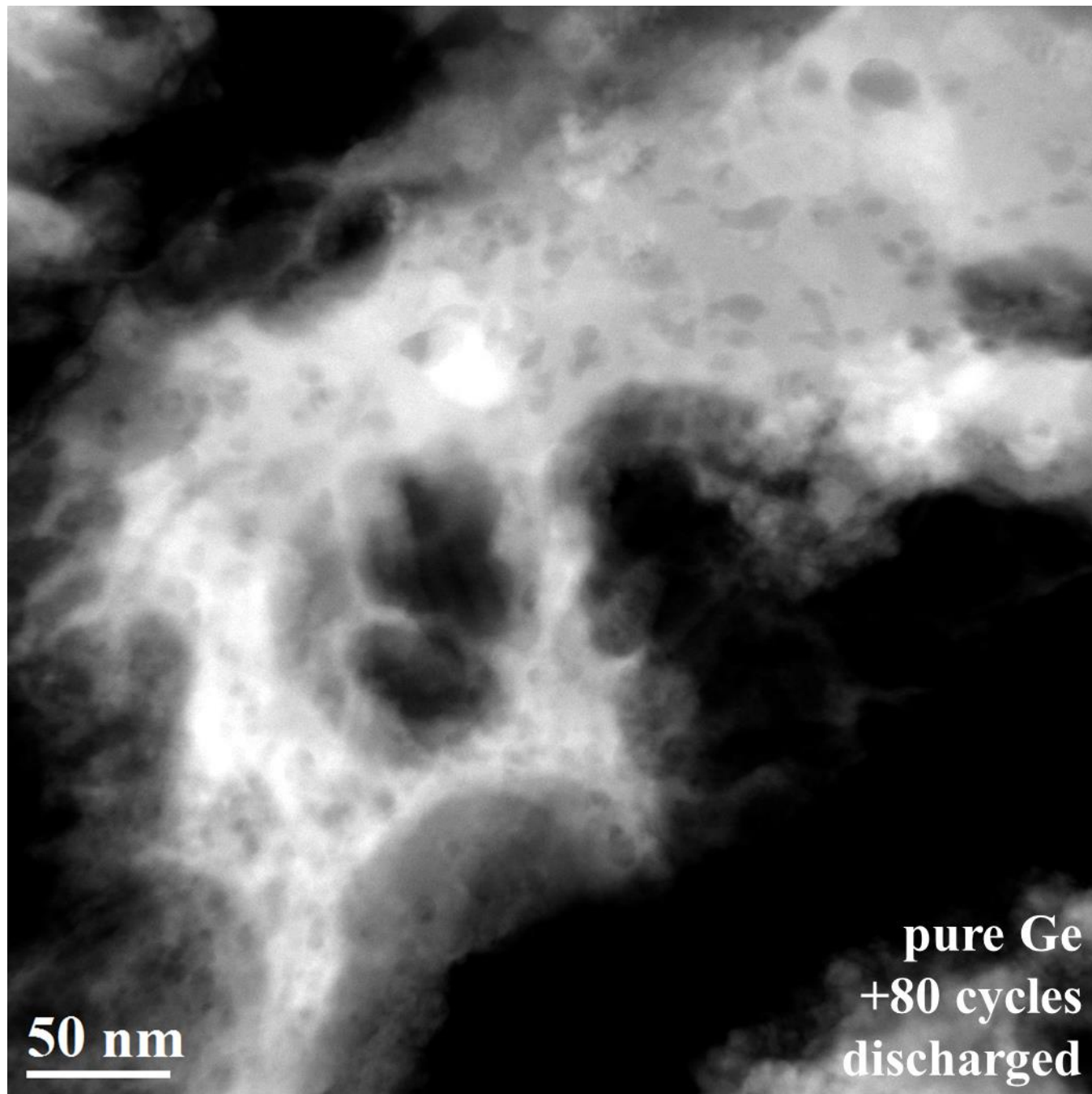
**Fig. S10.** SEM and EDS mapping of cycled electrodes (+80 cycles, after the variable *C*-rate test, charged state) with the pure Ge (SEM: a-c, EDS: g-l) or  $\text{Ge}_{0.9}\text{Se}_{0.1}$  (SEM: d-f, EDS: m-r) as the active material. The cycled pure Ge based electrodes show significant film delamination and significantly more dendritic growths (growing out of the pure Ge particles). The EDS mapping for the cycled (charged) pure Ge based electrode (g-l) shows a region with some Ge particles covered in dendritic growths and some comparatively clean of dendritic growths. The EDS mapping for the cycled (charged)  $\text{Ge}_{0.9}\text{Se}_{0.1}$  based electrode (m-r) shows that there are more dendritic growths observable in the charged state than in the discharged state.



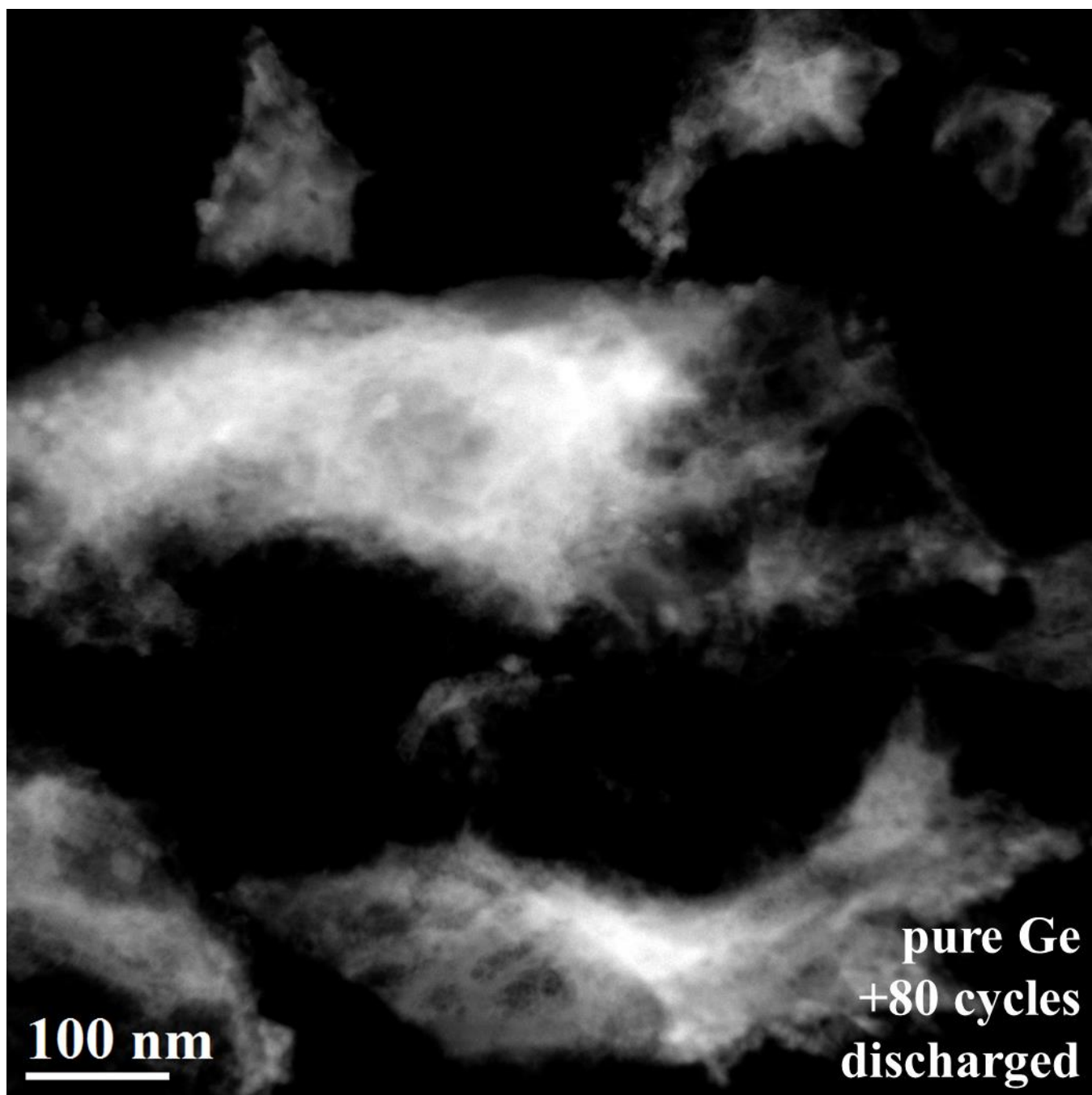
**Fig. S11.** *Ex-situ* TEM of ultramicrotome sectioned cycled (discharged) pure Ge-based electrode after the 80 cycle variable *C*-rate test. (a) TEM of Ge particle and (b) corresponding selected area electron diffraction pattern (SAED). The prominent reflections form rings corresponding to the dominant (111) and (022) planes of Ge. The small area shown in the HR-TEM image (c) cannot be observed exclusively by SAED given restrictions on the aperture size but from FFT (d) it is found that the crystalline structure visually apparent is also Ge.



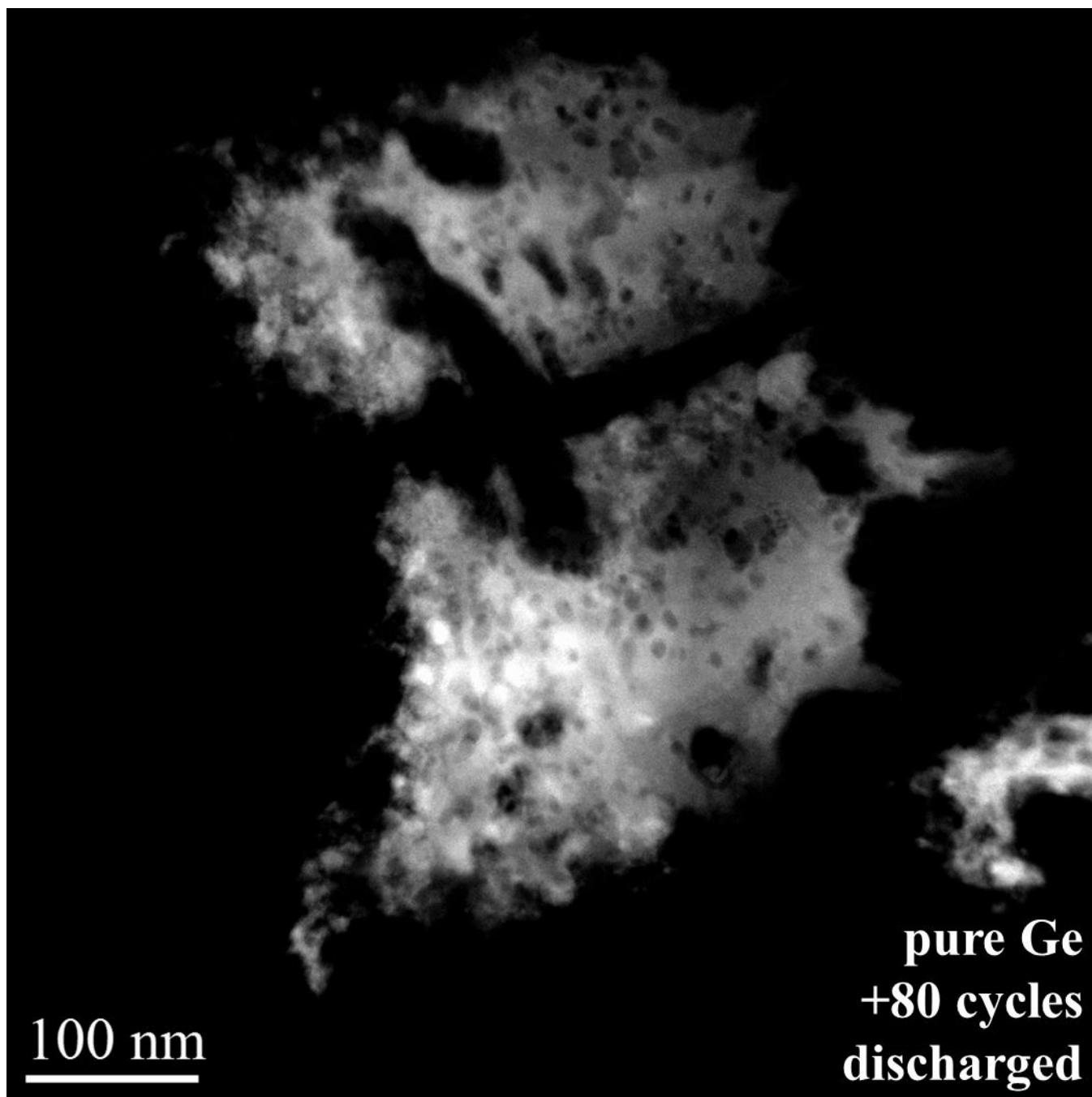
**Fig. S12a.** HAADF-STEM of a Ge particle from the pure Ge-based electrode in its discharged state after 80 cycles of variable *C*-rate testing. Note that the edges of the particle appear torn and fractured. There are several locations on the edge (perimeter) of the particle which appear to be half of a cavity, the hole-like structure observed throughout the interior of the particle.



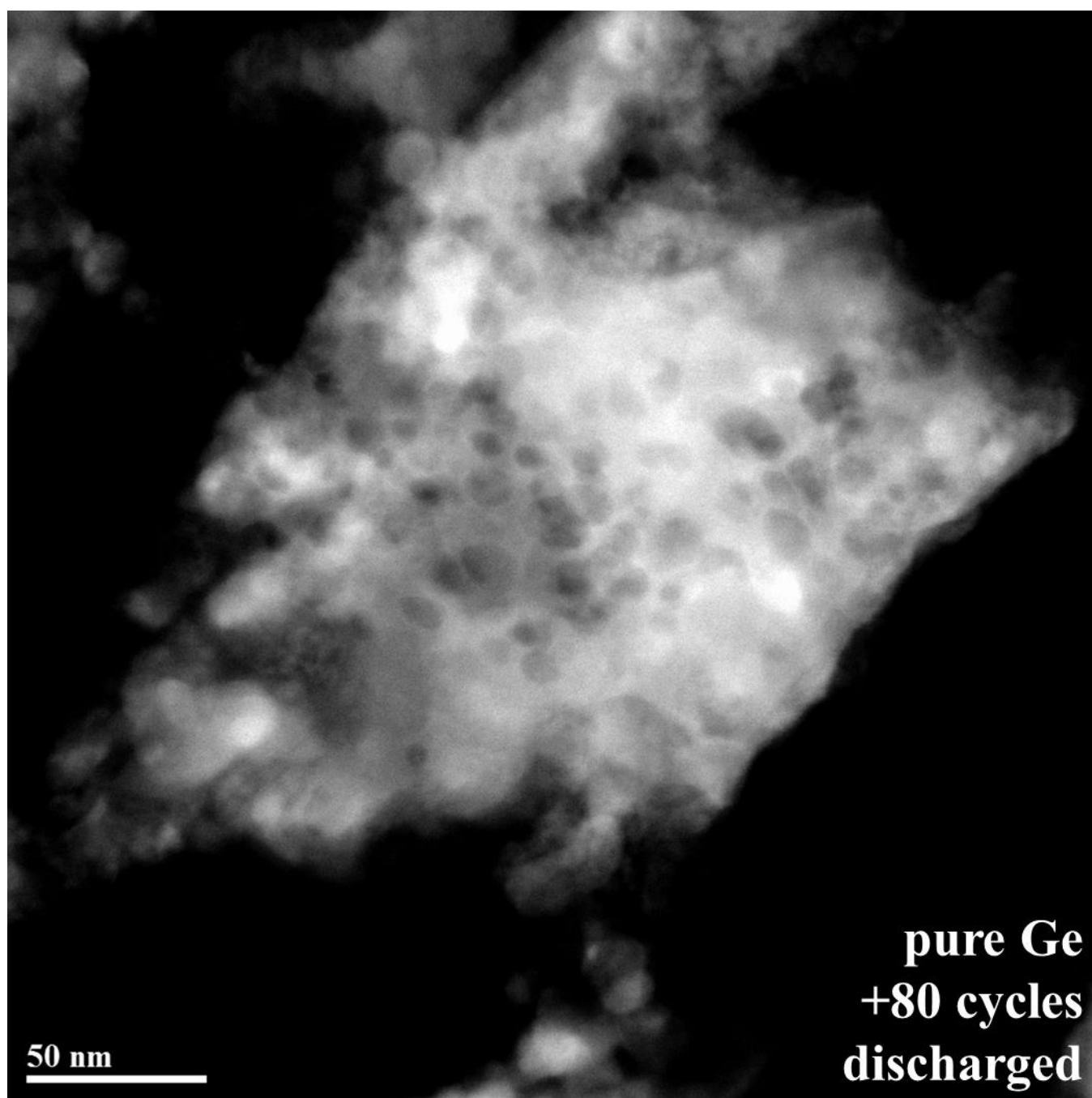
**Fig. S12b.** HAADF-STEM of a Ge particle from the pure Ge-based electrode in its discharged state after 80 cycles of variable C-rate testing. Note that the edges of the particle appear torn and fractured. There are several locations on the edge (perimeter) of the particle which appear to be half of a cavity, the hole-like structure observed throughout the interior of the particle.



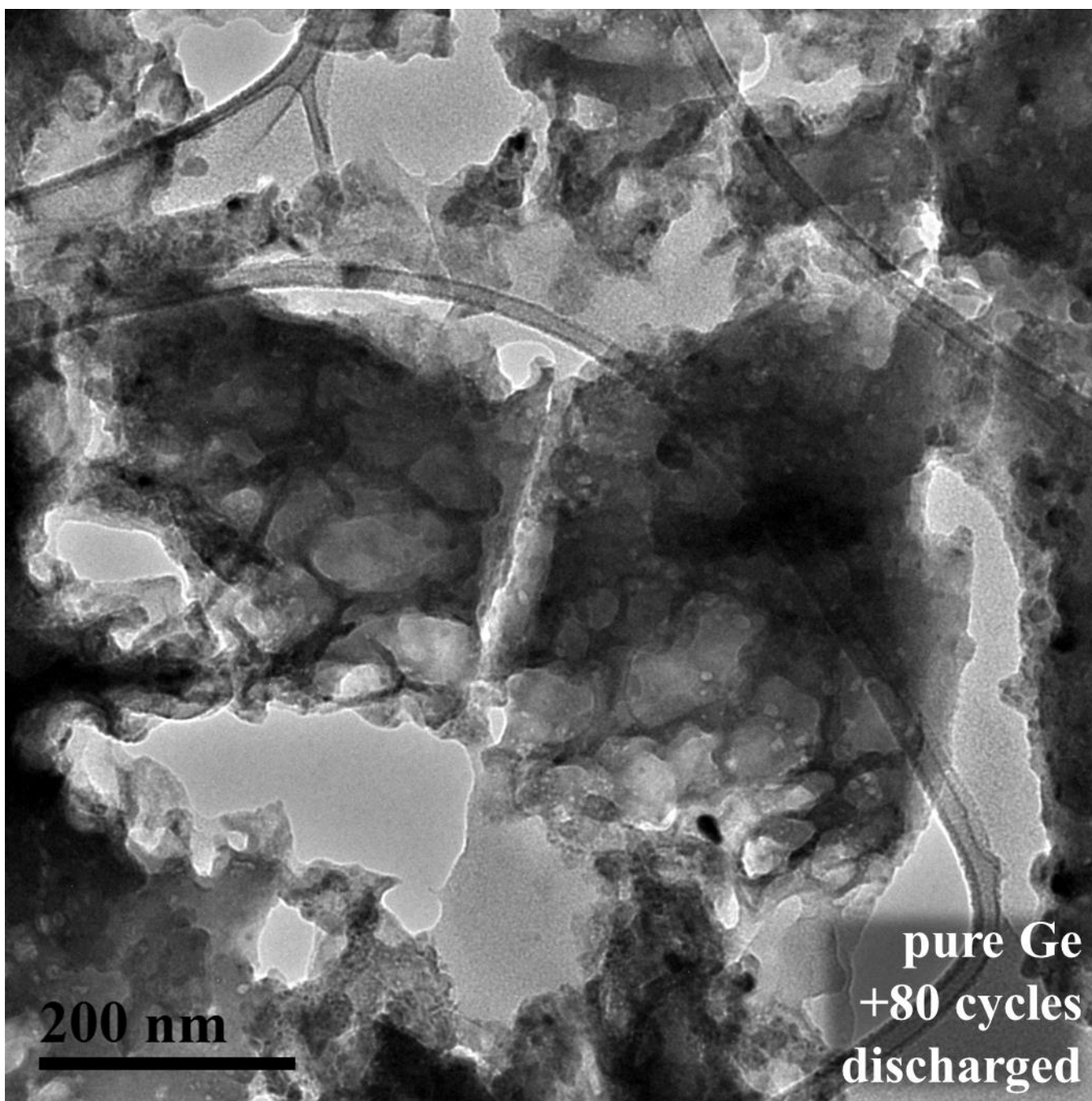
**Fig. S12c.** HAADF-STEM of a Ge particle from the pure Ge-based electrode in its discharged state after 80 cycles of variable *C*-rate testing. Note that the edges of the particle appear torn and fractured. There are several locations on the edge (perimeter) of the particle which appear to be half of a cavity, the hole-like structure observed throughout the interior of the particle.



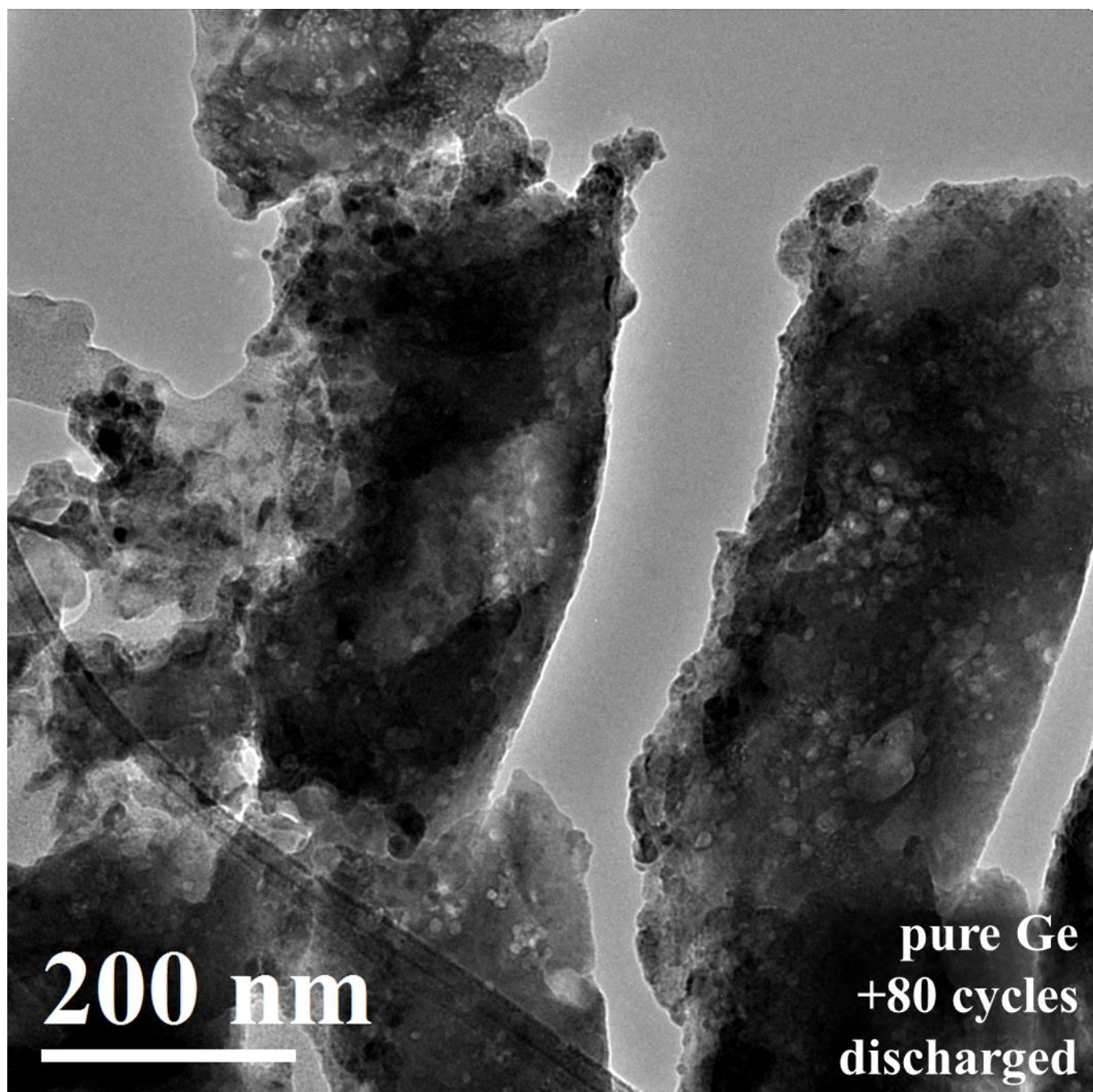
**Fig. S12d.** HAADF-STEM of a Ge particle from the pure Ge-based electrode in its discharged state after 80 cycles of variable *C*-rate testing. Note that the edges of the particle appear torn and fractured. There are several locations on the edge (perimeter) of the particle which appear to be half of a cavity, the hole-like structure observed throughout the interior of the particle.



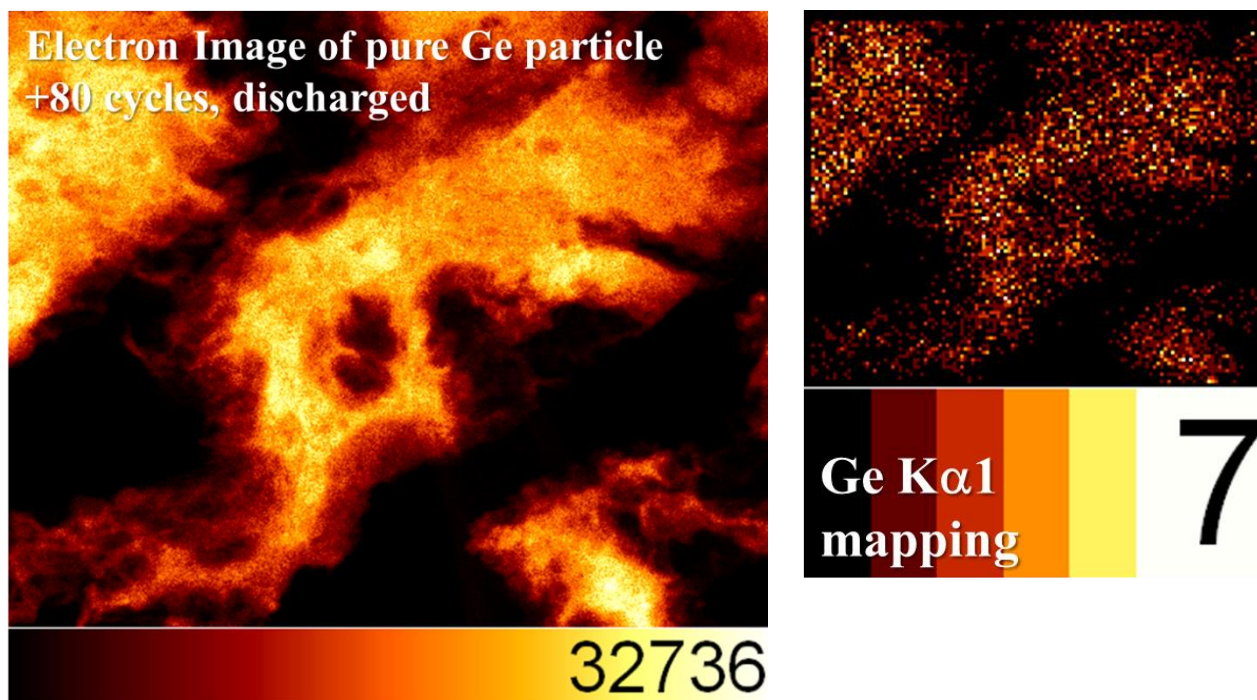
**Fig. S12e.** HAADF-STEM of a Ge particle from the pure Ge-based electrode in its discharged state after 80 cycles of variable *C*-rate testing. Note that the edges of the particle appear torn and fractured. There are several locations on the edge (perimeter) of the particle which appear to be half of a cavity, the hole-like structure observed throughout the interior of the particle.



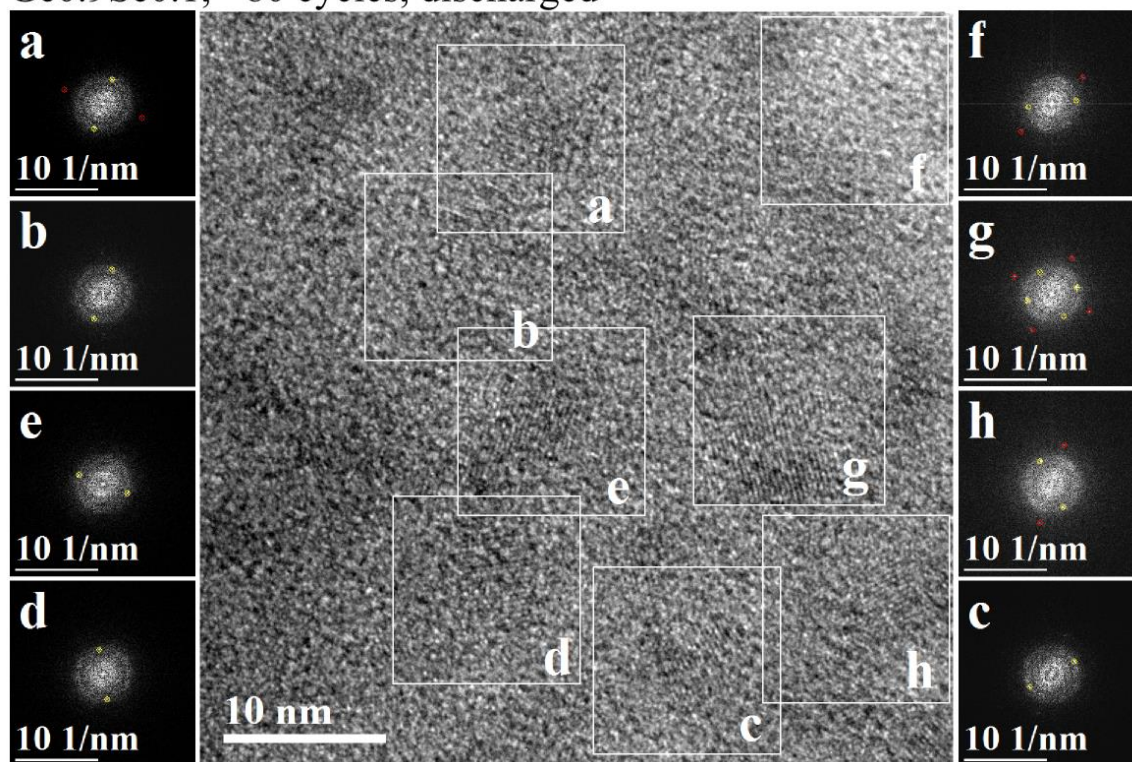
**Fig. S12f.** TEM of a Ge particle from the pure Ge-based electrode in its discharged state after 80 cycles of variable *C*-rate testing. Note that the edges of the particle appear torn and fractured. There are several locations on the edge (perimeter) of the particle which appear to be half of a cavity, the hole-like structure observed throughout the interior of the particle.



**Fig. S12g.** TEM of a Ge particle from the pure Ge-based electrode in its discharged state after 80 cycles of variable *C*-rate testing. Note that the edges of the particle appear torn and fractured. There are several locations on the edge (perimeter) of the particle which appear to be half of a cavity, the hole-like structure observed throughout the interior of the particle.



**Fig. S12h.** EDS mapping of a Ge particle from the pure Ge-based electrode in its discharged state after 80 cycles of variable *C*-rate testing. The mapping was done to further verify the identity of the particle being characterized by HR-TEM and/or HAADF-STEM. The electron image from the mapping is shown at left and the Ge K $\alpha$ 1 mapping is shown at right. Because the EDS detector does not have a drift corrector, similar mappings could not be performed at higher-magnifications.

Ge<sub>0.9</sub>Se<sub>0.1</sub>, +80 cycles, discharged

**Fig. S13.** FFT analysis of HR-TEM image of interior of Ge<sub>0.9</sub>Se<sub>0.1</sub> particle in discharged state after 80 cycle variable *C*-rate test. The FFT resolution is sufficient to identify only several out of all the visible crystallite regions in the image. The cycled material appears to be a network of nano-inclusions of Ge (crystalline in the discharged state) surrounded by an amorphous material.

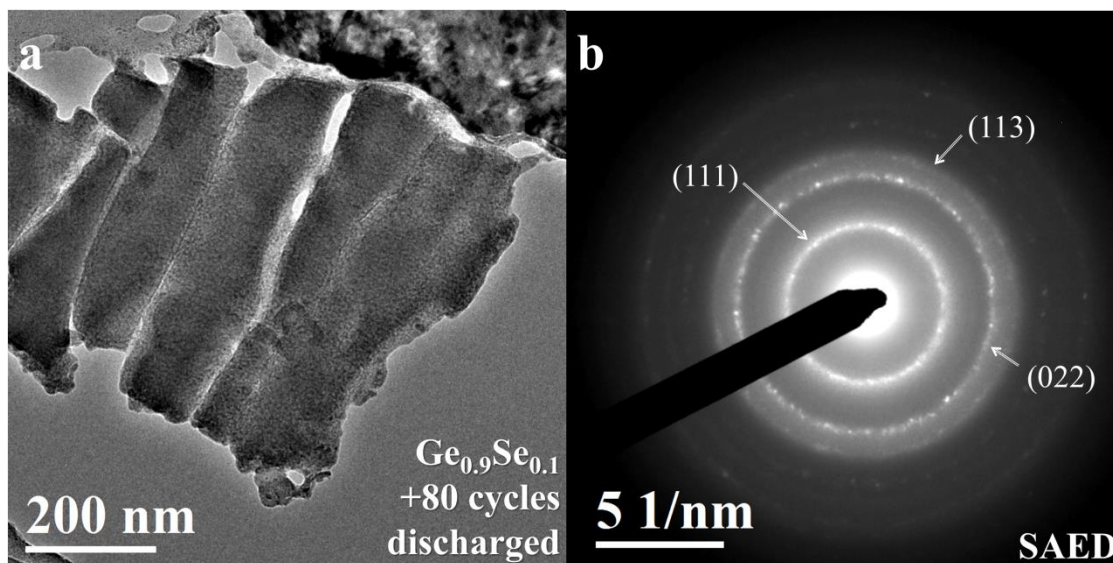


**Fig. S14.** SAED analysis of HR-TEM image of  $\text{Ge}_{0.9}\text{Se}_{0.1}$  particles in discharged state after 80 cycle variable *C*-rate test. Only reflections (rings, indicating polycrystalline material) for Ge planes are observed in the SAED. Surprisingly, no other reflections are visible, indicating that the Se in the particle is within an amorphous phase rather than in crystalline  $\text{Li}_2\text{Se}$ .

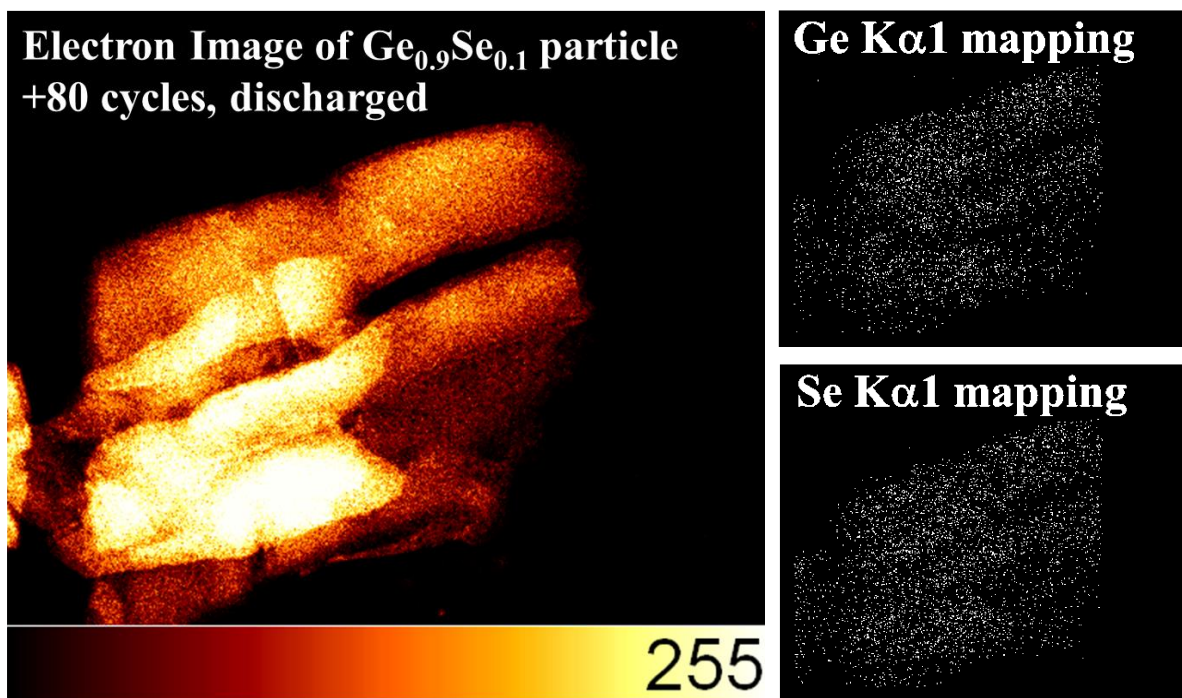


**Fig. S15.** EDS mapping of a  $\text{Ge}_{0.9}\text{Se}_{0.1}$  particle from the  $\text{Ge}_{0.9}\text{Se}_{0.1}$ -based electrode in its discharged state after 80 cycles of variable *C*-rate testing. The mapping was done to further verify the identity of the particle being characterized by HR-TEM and/or HAADF-STEM. The electron image from the mapping is shown at left and the Ge  $\text{K}\alpha_1$  and Se  $\text{K}\alpha_1$  mapping is shown at right. Because the EDS detector does not have a drift corrector, similar mappings could not be performed at higher-magnifications. However, the mapping and EDS spectra are sufficient to show that there is Se present in the particle. Useful quantitative analysis was precluded by the condition of the detector (not calibrated).

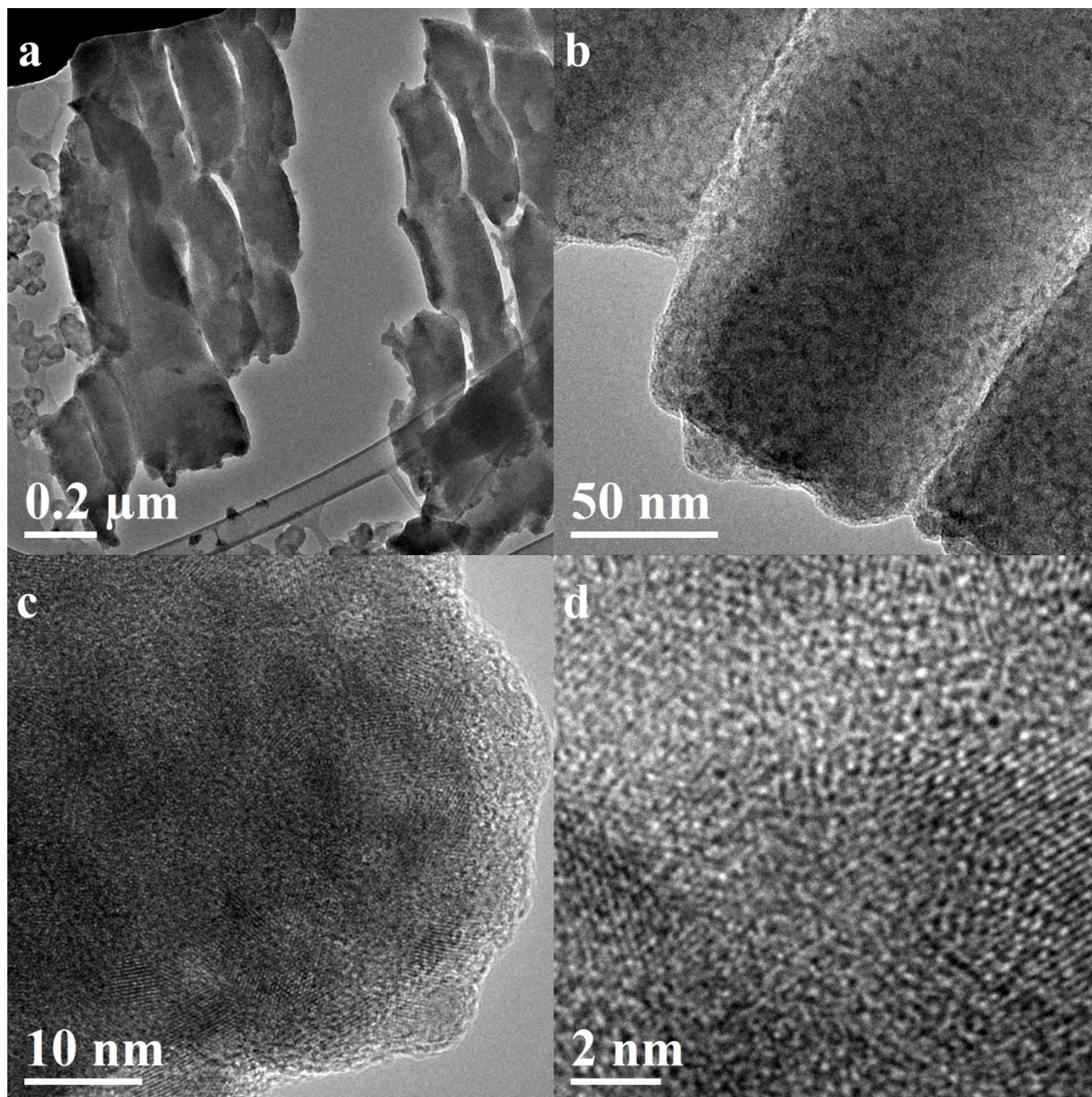


**Fig. S16.** HR-TEM of a  $\text{Ge}_{0.9}\text{Se}_{0.1}$  particle from the  $\text{Ge}_{0.9}\text{Se}_{0.1}$ -based electrode in its discharged state after 80 cycles of variable *C*-rate testing. Note that the edges of the particle appear to be relatively intact and have comparatively smooth edges, suggesting that the particles did not fracture. In (a) there may be evidence to suggest that the particles cleanly break, but because this seems to occur along parallel lines we believe this may be an artefact of the ultramicrotome sectioning technique. Within the particle, there are no pores or cavities and at progressively higher magnifications the network of nanocrystallite inclusions of Ge around small veins of an amorphous material are observed.

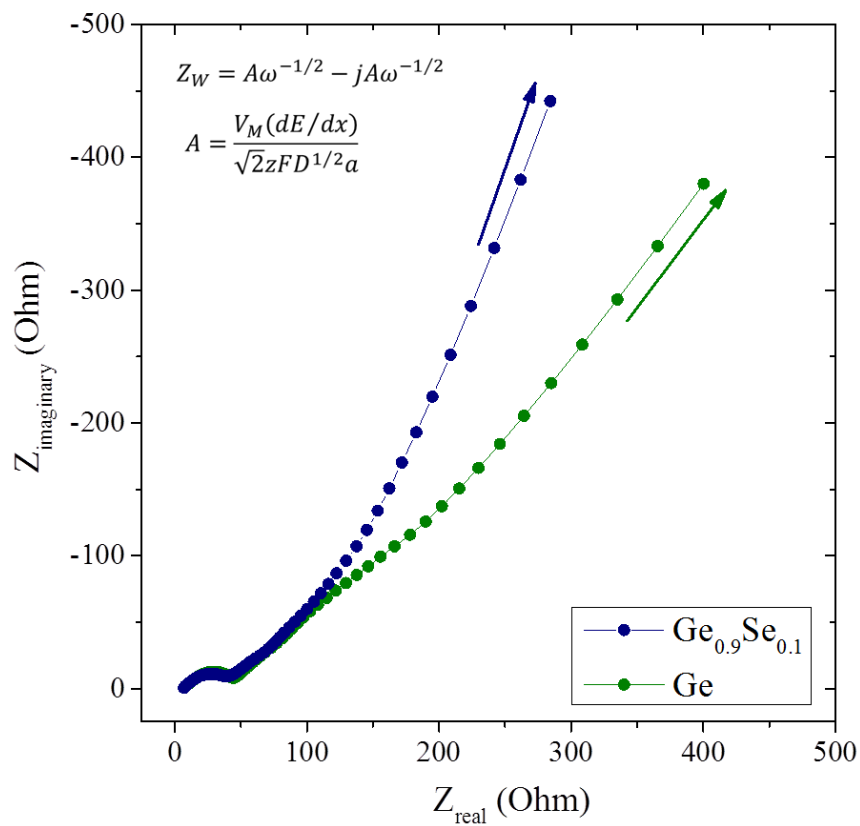


**Fig. S17.** EIS performed from 100 kHz to 0.01 Hz at open circuit potential on the pure Ge-based and the  $\text{Ge}_{0.9}\text{Se}_{0.1}$ -based electrodes at a state of full discharge following the 80 cycle variable C-rate test.

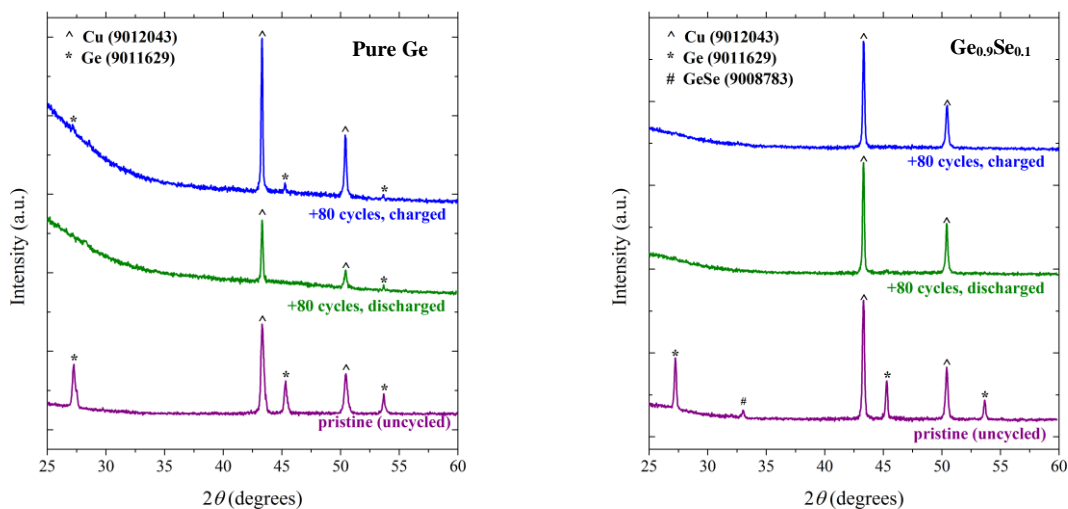


**Fig. S18.** *Ex-situ* XRD (Rikagu Microflex 600) of pristine and cycled pure Ge based or Ge<sub>0.9</sub>Se<sub>0.1</sub> based electrodes in the charged and discharged state after the 80-cycle variable *C*-rate test. Due to the nature of the experiment, two nominally identical electrodes (with very similar galvanostatic cycling performance) were used, one for the pattern of the charged electrode and one for the pattern of the discharged electrode. Interestingly, for the cycled pure Ge based electrode, a Ge pattern is observed for both the charged and discharged electrode. Although it is possible that the discharged electrode reverts into polycrystalline domains large enough to be identifiable by XRD, we believe that this pattern from the discharged state is more likely attributable to electrochemically disconnected, discharged pure Ge active material. With higher degree of confidence, we attribute the Ge pattern observed in the charged pure Ge based electrode to this phenomenon. In contrast, there is no Ge pattern observed in the charged or discharged Ge<sub>0.9</sub>Se<sub>0.1</sub> based electrodes. This indicates that the nanocrystallites of Ge characterized in the discharged electrode by HR-TEM, SAED and FFT are possibly too small or not strongly crystalline enough to form a clear XRD pattern. This odd behaviour has been observed previously in a similar study<sup>4</sup> which employed D-STEM, a powerful electron microscopy technique which enables the collection of an electron diffraction pattern from a point on the sample only 2 nm in diameter.

## Notes and references

<sup>a</sup> McKetta Department of Chemical Engineering, 200 E. Dean Keeton St. Stop C0400 Austin, TX 78712, USA.

<sup>b</sup> Texas Materials Institute, The University of Texas at Austin, Austin, TX 78712, USA.

<sup>c</sup> Department of Chemistry, 105 E. 24th St. Stop A5300 Austin, TX 78712, USA.

1. Ross, L.; Bourgon, M., Germanium-selenium phase diagram. *Can. J. Chem.* **1969**, *47* (Copyright (C) 2014 American Chemical Society (ACS). All Rights Reserved.), 2555-9. <http://dx.doi.org/10.1139/v69-422>
2. Klavetter, K. C.; Wood, S. M.; Lin, Y.-M.; Snider, J. L.; Davy, N. C.; Chockla, A. M.; Romanovicz, D. K.; Korgel, B. A.; Lee, J.-W.; Heller, A.; Mullins, C. B., A high-rate germanium-particle slurry cast Li-ion anode with high Coulombic efficiency and long cycle life. *Journal of Power Sources* **2013**, *238* (0), 123-136. <http://dx.doi.org/http://dx.doi.org/10.1016/j.jpowsour.2013.02.091>
3. Wang, D. Y.; Dahn, J. R., A High Precision Study of Electrolyte Additive Combinations Containing Vinylene Carbonate, Ethylene Sulfate, Tris(trimethylsilyl) Phosphate and Tris(trimethylsilyl) Phosphite in Li[Ni<sub>1/3</sub>Mn<sub>1/3</sub>Co<sub>1/3</sub>]O<sub>2</sub>/Graphite Pouch Cells. *Journal of The Electrochemical Society* **2014**, *161* (12), A1890-A1897. <http://dx.doi.org/10.1149/2.0841412jes>
4. Abel, P. R.; Klavetter, K. C.; Jarvis, K.; Heller, A.; Mullins, C. B., Sub-stoichiometric germanium sulfide thin-films as a high-rate lithium storage material. *Journal of Materials Chemistry A* **2014**, *2* (44), 19011-19018. <http://dx.doi.org/10.1039/c4ta04496g>
5. Frequently Asked Questions. <http://www.jetpulverizer.com/faq.php#link-7>.
6. JET PULVERIZER WORKS TO COMMERCIALIZE EMERGING LITHIUM-ION BATTERY TECHNOLOGY. <http://www.jetpulverizer.com/news-and-events/article01.php>.
7. Klavetter, K. C.; Snider, J. L.; de Souza, J. P.; Tu, H.; Cell, T. H.; Cho, J. H.; Ellison, C. J.; Heller, A.; Mullins, C. B., A free-standing, flexible lithium-ion anode formed from an air-dried slurry cast of high tap density SnO<sub>2</sub>, CMC polymer binder and Super-P Li. *Journal of Materials Chemistry A* **2014**, *2* (35), 14459-14467. <http://dx.doi.org/10.1039/c4ta03201b>